ADVANCES IN ATMOSPHERIC SCIENCES, 2021

• **Data Description Article** •

NUIST ESM v3 Data Submission to CMIP6

Jian CAO[1,2], Libin MA[3], Fei LIU[1,2], Jing CHAI[1,2], Haikun ZHAO[1], Qiong HE[1,2], Bo WANG[1,2], Yan BAO[1,2], Juan LI[1,2], Young-min YANG[1,2], Hua DENG[1,2], and Bin WANG[*2,4]

[1]*Key Laboratory of Meteorological Disaster, Ministry of Education/Joint International Research Laboratory of Climate and Environment Change/Collaborative Innovation Center on Forecast and Evaluation of Meteorological Disasters, Nanjing University of Information Science and Technology, Nanjing* 210044, *China*

[2]*Earth System Modeling Center, Nanjing University of Information Science and Technology, Nanjing* 210044, *China*

[3]*State Key Laboratory of Severe Weather, Chinese Academy of Meteorological Sciences, Beijing* 100081, *China*

[4]*Department of Atmospheric Sciences, University of Hawaii at Manoa, Honolulu, HI* 96825, *USA*

(Received 16 June 2020; revised 19 October 2020; accepted 29 October 2020)

ABSTRACT

This paper introduces the experimental designs and outputs of the Diagnostic, Evaluation and Characterization of Klima (DECK), historical, Scenario Model Intercomparison Project (MIP), and Paleoclimate MIP (PMIP) experiments from the Nanjing University of Information Science and Technology Earth System Model version 3 (NESM3). Results show that NESM3 reasonably simulates the modern climate and the major internal modes of climate variability. In the Scenario MIP experiment, changes in the projected surface air temperature (SAT) show robust "Northern Hemisphere (NH) warmer than Southern Hemisphere (SH)" and "land warmer than ocean" patterns, as well as an El Niño-like warming over the tropical Pacific. Changes in the projected precipitation exhibit "NH wetter than SH" and "eastern hemisphere gets wetter and western hemisphere gets drier" patterns over the tropics. These precipitation patterns are driven by circulation changes owing to the inhomogeneous warming patterns. Two PMIP experiments show enlarged seasonal cycles of SAT and precipitation over the NH due to the seasonal redistribution of solar radiation. Changes in the climatological mean SAT, precipitation, and ENSO amplitudes are consistent with the results from PMIP4 models. The NESM3 outputs are available on the Earth System Grid Federation nodes for data users.

Key words: NESM3, CMIP6, Scenario MIP, PMIP

Citation: Cao, J., and Coauthors, 2021: NUIST ESM v3 Data Submission to CMIP6. *Adv. Atmos. Sci.*, https://doi.org/10.1007/s00376-020-0173-9. (in press)

1. Introduction

Since the launch of the Coupled Model Intercomparison Project (CMIP) in 1995, participating model simulations have not only attracted tremendous attention from the scientific community (Meehl et al., 2000) but also provided scientific guidance for the Intergovernmental Panel on Climate Change (IPCC) (e.g., IPCC, 2013). Phase 6 of CMIP (CMIP6) was recently launched and has registered over 100 model versions. It has designed a handful of basic experiments, proposed an ensemble of endorsed Model Intercomparison Projects (MIPs), and defined the structure of model outputs to address the scientific questions proposed by the World Climate Research Program (Eyring et al., 2016). In particular, CMIP6 endorses over 20 MIPs, which focus on more specific scientific targets (Eyring et al., 2016).

The Nanjing University of Information Science and Technology Earth System Model (NUIST-ESM, or NESM) is a new member of the CMIP community. The development of NESM dates back to 2012, and the first version of NESM was released in 2014. It couples the ECHAM v5.3, NEMO v3.4, and CICE v4.1 via the OASIS_3.0-MCT coupler (Cao et al., 2015). NESM v1 was widely used to study global monsoon dynamics and predictability, tropical cyclone dynamics, and paleoclimate formation (e.g., Wang et al., 2018; Cao et al., 2019a, b). The subsequent version of NESM, NESM v2, targeted an improvement in the understanding of seasonal predictability. To better facilitate CMIP6, a more comprehensive model version was developed: NESM v3 (NESM3), which has upgraded atmospheric and land-surface model components, improved ocean–ice coupling, and increased model resolutions (Cao et al., 2018; Ma et al., 2020). NESM3 has registered the Diagnostic, Evaluation

* Corresponding author: Bin WANG
Email: wangbin@hawaii.edu

© The Authors [2021]. This article is published with open access at link.springer.com.

and Characterization of Klima (DECK), historical simulation, and serval other CMIP6-endorsed MIPs.

The DECK run includes the Atmospheric MIP (AMIP) simulation, pre-industrial (PI) experiment, abrupt quadrupling of CO_2 (abrupt4×CO2) experiment, and 1%yr^{-1} CO_2 increase (1pctCO2) experiment. The DECK and historical simulations are regarded as the baseline experiments of CMIP6. In this study, we systematically introduce the activities of NESM3 in the DECK, historical simulation, Scenario MIP, and Paleoclimate MIP (PMIP) experiments. These experiments are used to validate and measure NESM3's performances in reproducing the modern climate and its responses to different external forcing.

The CMIP6 Scenario MIP is driven by the forcing from the Shared Socioeconomic Pathways (SSPs), which are more closely linked to societal concerns compared to their counterparts in previous phases (Eyring et al., 2016; O'Neill et al., 2016). Five types of SSPs (i.e., SSP1–5) are designed in the Scenario MIP. Each SSP is an integrated scenario that describes human development, economic growth, investments in education and health, and future energy planning and land-use changes (O'Neill et al., 2016). The results of SSPs could be compared with the results from the Representative Concentration Pathways (RCPs) of CMIP5 using the criterion of the same long-term global averaged radiative forcing level. Multi-optional experiments are suggested in Scenario MIP to facilitate the cooperation between Scenario MIP and other MIPs.

The MH and Last Interglacial (LIG) periods are the two most recent warm periods in Earth's history (Otto-Bliesner et al., 2017). The MH and LIG are ~6 and ~127 ka before present, respectively. Paleo-data synthesis has revealed the changes in the global climate and environment relative to the modern climate. The changes are mainly attributed to external forcing of the Earth's orbital parameters, which induces incoming solar radiation redistribution (Capron et al., 2017; Hoffman et al., 2017). The two periods are often discussed analogously with future climate changes due to anthropocentric warming (Yin and Berger, 2015). Both model–proxy data and model–model comparison studies have contributed to climate model evaluation and understanding of climate changes (e.g., Scussolini et al., 2019), especially for the MH simulation explicitly designed since the first phase of CMIP (Joussaume and Taylor, 1995).

So far, NESM3 has completed the DECK, historical, Scenario MIP, and PMIP experiments, and the outputs are available to users. In section 2, we present the model configuration and detailed experimental designs of all simulations. Preliminary evaluation of model results is shown in section 3, data submissions are introduced in section 4, and conclusions are given in section 5.

2. Model and experimental design

2.1. *Model description*

NESM3 consists of three component models, which are coupled by the OASIS_3.0-MCT3 coupler (Valcke et al., 2015). The atmospheric component model of NESM3 is ECHAM v6.3, which implicitly couples the JSBACH land-surface model (Giorgetta et al., 2013). The ocean and sea-ice component models are NEMO v3.4 (Madec and the NEMO team, 2012) and CICE v4.1 (Hunke and Lipscomb, 2010), respectively.

NESM3 includes two subversions—namely, standard resolution and lower resolution. The standard resolution NESM3 is used to perform all CMIP6 experiments. The resolution of the atmospheric component model is T63L47, which corresponds to ~1.9° × ~1.9°, and 47 vertical layers extending from the surface to 0.01 hPa. The ocean component model uses the ORCA1 configuration, which is a tripole grid system. The horizonal resolution is ~1° in both longitudinal and latitudinal directions, with meridional refinement to 1/3° near the equator. There are 46 vertical layers in the ocean model, with 10 layers in the uppermost 100 m. The CICE model is configured in a displaced-polar grid system, with its horizontal resolution of the sea-ice model being ~1° and ~0.5° in longitudinal and latitudinal directions, respectively. CICE v4.1 solves the dynamic and thermodynamic equations for five categories of ice thickness. Detailed model description and model development can be found in Cao et al. (2018).

2.2. *CMIP6 forcing for NESM3*

In NESM3 CMIP6 activities, all forcings follow the CMIP6 experimental designs and can be downloaded from https://esgf-node.llnl.gov/search/input4mips/. The monthly mean values of globally averaged long-lived and well-mixed greenhouse gas (GHG) concentrations are used in NESM3. The aerosol-radiative effect of the anthropogenic aerosol is prescribed by the spatiotemporally distributed optical depth, symmetry factor, and single scattering albedo, while only the Twomey effect (Twomey, 1977) is considered in the cloud–aerosol interaction effect in NESM3. The change in stratospheric aerosol is only considered by the three-dimensionally distributed ozone concentration. The monthly mean land-surface forcing (land use and land cover) and solar forcing are also used.

2.3. *Experimental design of DECK and historical experiments*

The initial conditions (ICs) for the ocean and land-surface models are critical for accelerating the coupled model spin-up process. In NESM3, the IC of the ocean model is from a 2000-year ocean model standalone integration forced by modern climatology. The IC of the land-surface model is from MPI-ESM-LR (Brovkin et al., 2013), which uses the same land-surface model as in NESM3. The ICs for the atmospheric model and sea-ice model are from modern observations. In the spin-up and production integrations of the PI experiment, the Earth orbital parameters, ozone concentration, GHG concentrations, and land-surface condition are the values in 1850, while the solar constant, natural tropospheric aerosol, and stratospheric aerosol forcing are the

decadal-averaged values of the 1850s. We conducted a 500-year simulation for the PI experiment after a 700-year spin-up (Table 1).

Two CO_2 experiments, 1pctCO2 and abrupt4×CO2, were conducted and launched from the PI experiment, except for the difference in CO_2 concentration. The 1pctCO2 experiment is forced by 1%yr^{-1} of CO_2 concentration increase during the whole 150-year integration. In the abrupt4×CO2 experiment, the CO_2 concentration is abruptly quadrupled and then held constant during the 150-year integration (Table 1).

As one of the CMIP6 standard experiments, the community explicitly defined the external forcing for the historical experiment (Eyring et al., 2016). Five types of external forcing are used to drive NESM3, including monthly mean globally averaged GHG concentrations, global land-use and land-cover forcing, solar irradiance, prescribed aerosol optical properties and change of cloud droplet effective radius fraction, and prescribed ozone concentration. The time-lag method is used to initialize the five ensembles of the historical experiments with different ICs from the PI experiment (Table 1). Five AMIP experiments were initialized by the atmospheric ICs from the corresponding realization of the historical experiments. The sea surface temperature (SST) and sea-ice concentration were obtained from the Program for Climate Model Diagnosis and Intercomparison. The integrations of all AMIP experiments span from 1975 to 2014, and the outputs from 1979 to 2014 have been submitted (Table 1).

2.4. *Experimental design of the Scenario MIP experiment*

In Scenario MIP, we considered three types of Tier-1 experiments—namely, SSP1-2.6, SSP2-4.5 and SSP5-8.5 as our priority. These scenarios are the successors to RCP2.6, RCP4.5 and RCP8.5 in CMIP5, respectively. Two ensemble members of each experiment were conducted, which were initialized at the end of realizations 1 and 2 of the historical experiments, respectively. The simulations span from 2015 to 2100 (Table 1). In addition to solar radiation and volcanic forcing, other external forcings are different in the SSP experiments. Volcanic forcing uses the same values as those in the PI experiment. The same suite of temporally evolving solar radiation forcing is used in all SSP experiments. All scenario experiments are also driven by the land-surface forcing, stratospheric aerosol and anthropogenic aerosol forcing, and globally averaged long-lived GHG concentrations of each scenario as designed in O'Neill et al. (2016).

2.5. *Experimental design of the PMIP experiment*

The registered MH and LIG experiments are the Tier-1 experiments of PMIP4/CMIP6 (Otto-Bliesner et al., 2017). Compared to the PI experiment, two types of external forcing, Earth's orbital parameters and GHG concentrations, are considered in the designs of the MH and LIG experiments (Table 2). All other boundary conditions (e.g., land–sea configuration, ice sheets) are identical to those of the CMIP6 PI experimental design (Table 2). Both the MH and LIG experiments branch from the PI experiment, and an

Table 1. Information on the experimental designs.

Experiment type	Experiment name	Length (period)	Ensemble size
DECK	AMIP	35 yr (1979–2014)	5
	piControl	500 yr	1
	abrupt4×CO2	150 yr	1
	1pctCO2	150 yr	1
Historical	Historical	165 yr (1850–2014)	5
ScenarioMIP	SSP1-2.6	86 yr (2015–2100)	2
	SSP2-4.5	86 yr (2015–2100)	2
	SSP5-8.5	86 yr (2015–2100)	2
PMIP	MH	100 yr	1
	LIG	100 yr	1

Table 2. Forcing and boundary conditions for the PI, MH and LIG experiments.

	PI	MH	LIG
Eccentricity	0.016724	0.018994	0.018682
Obliquity (°)	23.446	24.105	24.04
Perihelion-180 (°)	102.04	0.87	275.41
CO_2 (ppm)	284.725	264.4	275
CH_4 (ppb)	791	597	685
N_2O (ppb)	275	262	255
Ice sheets	Modern	Modern	Modern
Land–sea configuration	Modern	Modern	Modern
Date of vernal equinox	21 March at noon	21 March at noon	21 March at noon

additional 500-year spin-up is conducted before the 100-year integration of each experiment. The outputs of the two experiments follow the requirements of PMIP4.

2.6. *Observational data*

The observational data used for model evaluation in this study are as follows: (1) monthly mean precipitation data of GPCP, version 2.2 (Huffman et al., 2009); (2) SST and sea-ice concentration data from HadISST (Rayner et al., 2003); (3) surface air temperature (SAT) from NCEP-2 (Kanamitsu et al., 2002); and (4) surface temperature anomalies from HadCRUT4 (Morice et al., 2012).

3. Results from DECK, historical and Scenario MIP experiments

A reasonable coupled system response to the temporally evolving external forcing requires the coupled model to realistically reproduce the complex feedbacks among the atmosphere, land surface, hydrosphere, cryosphere, and biosphere. To this end, the performance of NESM3 is evaluated in terms of the climatological mean states and atmosphere–sea-ice–ocean interaction phenomena among the model components for the modern climate. With respect to future climate change, changes in the warming magnitudes, large-scale features (e.g., surface temperature, precipitation, and monsoon), and related Earth system internal modes (e.g., ENSO and MJO) under different scenarios are the main concern (e.g., Collins et al., 2013). Thus, the projected global mean surface temperature (GMST), Northern Hemisphere (NH) sea-ice extent (SIE), anomalies in SAT and precipitation, ENSO behavior, and MJO in the SSP1-2.6, SSP2-4.5, and SSP5-8.5 experiments are discussed in this study.

3.1. *Equilibrium climate sensitivity and transient climate response*

The equilibrium climate sensitivity (ECS) and transient climate response (TCR) are used to demonstrate the responses of a coupled model to abrupt and transient CO_2 forcing. ECS is defined as the GMST change due to forcing in the form of an abrupt doubling of CO_2 after reaching the new equilibrium state. ECS values estimated by the Gregory method (Gregory et al., 2004) show a continuous increase from CMIP3 to CMIP6; particularly, there is a substantial change from 3.31 ± 0.74 K in CMIP5 models to 3.86 ± 1.10 K in CMIP6 models (Flato et al., 2013; Zelinka et al., 2020). The abrupt4×CO2 experiment predicts an equilibrium temperature change of 9.4 K when the Earth reaches the new equilibrium state (Fig. 1a). This means that the ECS is 4.7 in NESM3, which is larger than most CMIP5/6 models (Flato et al., 2013; Meehl et al., 2020).

TCR is regarded as the averaged GMST change during years 60–80 in the 1pctCO2 experiment. Previous studies have shown that the high-ECS models have high TCR values in CMIP5/6 models (Flato et al., 2013; Meehl et al., 2020). The TCR of NESM3 is 2.8 K (Fig. 1b), which is higher than that of most CMIP6 models (Meehl et al., 2020).

3.2. *Evolution of GMST and SIE*

As one of the most concerning factors for the historical simulation, the simulated GMST time series are first discussed and compared with the HadCRUTv4 observation. Figure 2a shows the GMST anomalies in five historical simulations, the historical ensemble mean, and the observed GMST anomalies relative to 1961–90. NESM3 simulates the temporal evolution of GMST very well, such as the significant global warming trend in recent decades, the warming hiatus around the 1950s, and the cooling response of surface temperature to large volcanic eruptions. The simulated GMST in the historical ensemble mean increases by 0.52°C in 1985–2014 compared to the preindustrial period (1850–79). The warming magnitude is 0.21°C less than the observation. This is mainly due to the warmer bias before the 1940s

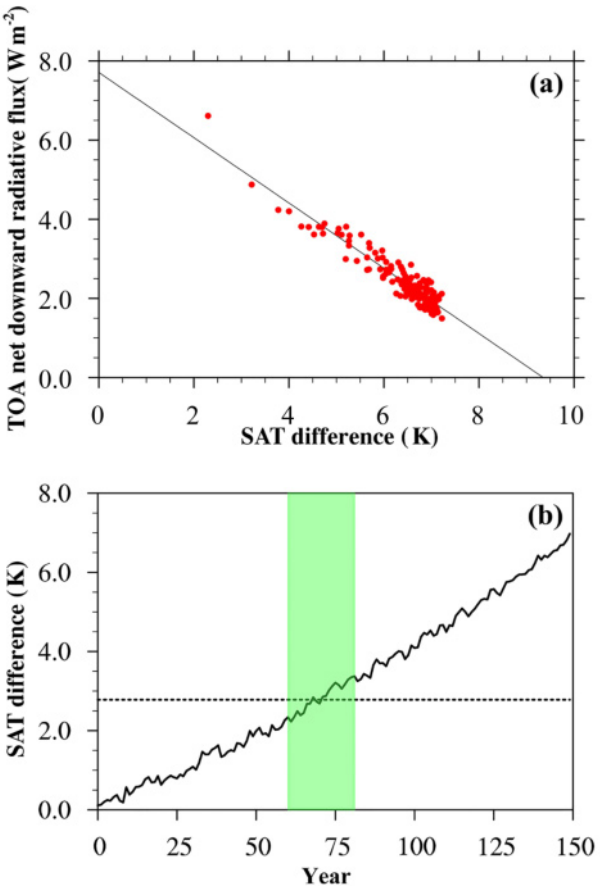

Fig. 1. The calculations of ECS and TCR from the abrupt4×CO2 experiment and 1pctCO2 experiment, respectively: (a) Relationship between the annual mean TOA net downward radiative flux and GMST anomalies relative to the PI experiment. The solid line represents the linear least-squares regression fit to the 150 years of model outputs. It predicts the equilibrium temperature change of 9.4 K, yielding an ECS of 4.7 K. (b) GMST response forcing in the form of a 1% per year increase in CO_2. The average temperature anomaly between years 60–80 (marked by green shading) is defined as the TCR. The dashed line shows the TCR value.

(Fig. 2a). Model results show the ensemble spread is small when the external forcing is large, e.g., the volcanic eruption years.

Figure 2b shows the projected GMST evolution in realizations 1 and 2 of the historical experiments and the SSP1-2.6, SSP2-4.5 and SSP5-8.5 experiments. The warming of GMST is similar for the three scenarios from 2015 to 2035. Regarding the SSP1-2.6 scenario, both realizations show a GMST peak at around 2060 and a slight decay before 2100.

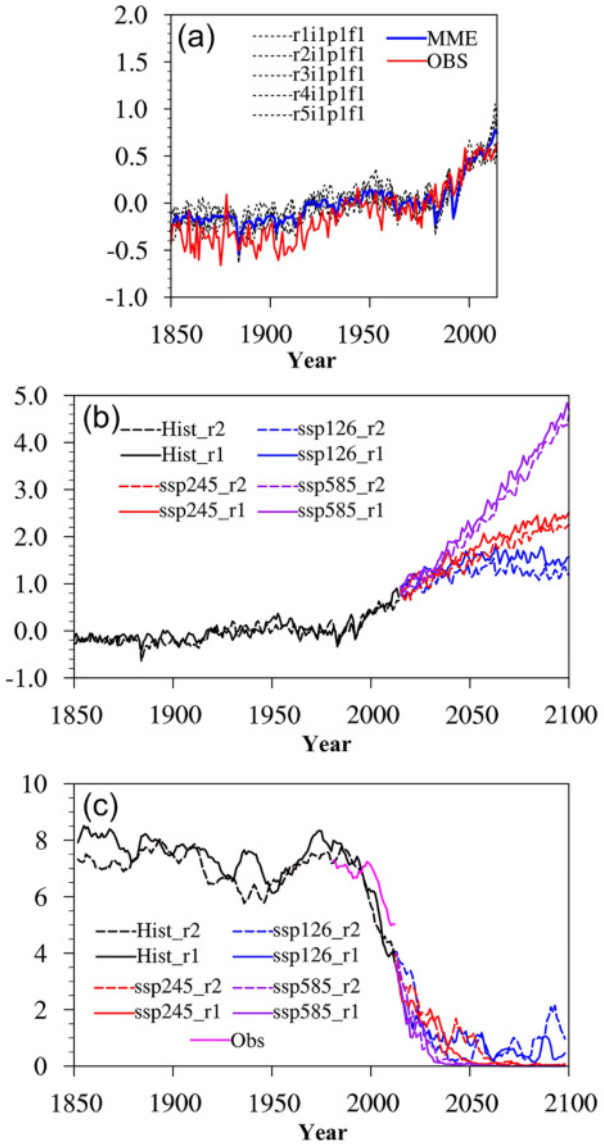

Fig. 2. Time series of global mean quantities: (a) GMST (unit: ℃) from observation (red), five historical experiments (dashed black), and the MME mean (blue). (b) GMST (unit: ℃) from realizations 1 and 2 of the historical experiments (black), SSP1-2.6 experiments (blue), SSP2-4.5 experiments (red), and SSP5-8.5 experiments (purple). The reference period for the GMST is 1961–90. (c) September Arctic SIE (units: 10^6 km^2) from realizations 1 and 2 of the historical experiments (black), SSP1-2.6 experiments (blue), SSP2-4.5 experiments (red), and SSP5-8.5 experiments (purple). The observed SIE is shown in magenta.

This is consistent with the experimental design of SSP1-2.6, which has a decline of radiative forcing in the middle of this century (O'Neill et al., 2016). Both the SSP2-4.5 and SSP5-8.5 experiments show a continuous increase of GMST during this century. During 2079–2100, the simulated GMSTs show an increase of 1.6°C, 2.4°C and 4.1°C in the ensemble mean of the SSP1-2.6, SSP2-4.5 and SSP5-8.5 experiment, respectively, relative to 1850–79.

Observations reveal an accelerated decline of the NH summer sea-ice coverage in recent decades (Overland and Wang, 2013). The projected summertime Arctic SIEs in all SSP experiments are shown in Fig. 2c. NESM3 can reproduce the accelerated decay of SIE during the past three decades (1985–2014). The simulated SIE decreases by about 50% from 1985 to 2014, which is slightly higher than the observation (Fig. 2c). The shrinkage of SIE is shown to be more rapid in the ensuing decades, proceeding to a sea-ice-free summer in all SSP experiments. A sea-ice-free summer is projected to be reached by around 2034, 2036 and 2027 in SSP1-2.6, SSP2-4.5 and SSP5-8.5, respectively. Here, a sea-ice-free summer is defined as the first time that the 5-year running mean SIE is less than 1×10^6 km^2 (Massonnet et al., 2012). The sea-ice-free timing is earlier than the estimate from CMIP5 RCP experiments (Massonnet et al., 2012; Jahn et al., 2016).

3.3. *Climatological temperature and precipitation*

For the modern-day mean state evaluation, we compare the model results of the last 30 years (1985–2014) from the historical experiment with the observation. All the mean states are derived from the ensemble mean of the five historical simulations, while the result from ensemble 1 of the historical experiment is used in the evaluation of interannual variation.

Figure 3 presents NESM3's ability to reproduce the observed SAT, and shows the patterns of SAT changes in the SSP1-2.6, SSP2-4.5 and SSP5-8.5 experiments relative to 1985–2014. The ensemble mean of the five historical experiments can successfully reproduce the observed temperature distribution, with the bias being within 1°C (2°C) over most of the ocean (land) (Figs. 3a–c). The simulated surface temperature is colder than the observation over the central-eastern equatorial Pacific, and the major cold bias centers are located over the high-latitude Atlantic Ocean and Antarctica. There is a warm bias over the Southern Ocean, mid-latitude Asia, and tropical northern Africa (Fig. 3c). The SAT biases over the high-latitude oceans are closely associated with the biases of excessive SIE over the Arctic and deficient SIE around Antarctica (not shown).

For the three global warming experiments, the patterns of SAT anomalies are similar, except for differences in magnitude. The SAT warming pattern is characterized by a warmer NH than SH and warmer land than ocean. The hemispheric temperature contrasts are more evident over the higher latitudes than the lower latitudes (Figs. 3d–f). That is, the temperature contrast between the hemispheres will be enlarged under future global warming. Over the tropics, the

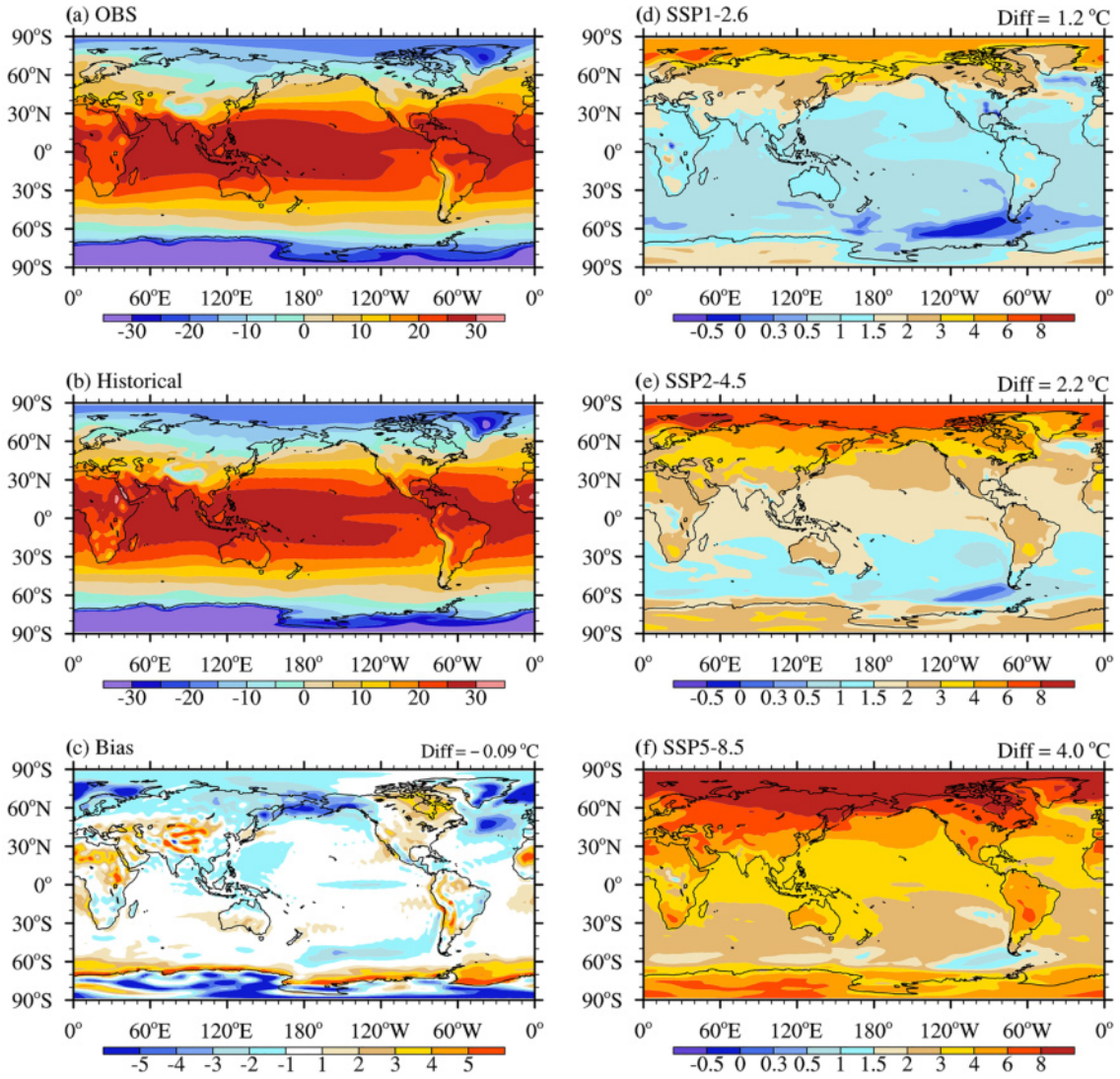

Fig. 3. Climatological mean surface air temperature (units: ℃) in the (a) observation, (b) ensemble mean of five historical experiments, and (c) their differences. (d–f) Changes in SAT from the ensemble mean of the (d) SSP1-2.6, (e) SSP2-4.5 and (f) SSP5-8.5 experiments relative to the simulated modern climatology (1985–2014) from the historical experiment.

projected SAT change is larger over the eastern equatorial Pacific than over the western equatorial Pacific. In summary, the projected SAT change is dominated by "warmer NH than SH" and "warmer land than ocean" patterns, as well as an El Niño-like warming over the tropics. Note that the subpolar Atlantic Ocean is relatively less warm than most of the globe. This so-called Atlantic "warming hole" is also shown by many CMIP5 RCP4.5 experiments (Collins et al., 2013).

The simulated annual mean precipitation during 1985 to 2014 is compared with the observation (Figs. 4a–c). NESM3 can reproduce well the large-scale feature of observed precipitation. The simulated major heavy precipitation regions are located in the Intertropical Convergence Zone (ITCZ), South Pacific Convergence Zone, and the mid-latitude storm-track regions. However, the model still suffers from double-ITCZ precipitation biases. Meanwhile, extensive precipitation appears over the upwind side of the mountain, and a dry bias dominates over the Amazon region. Surprisingly, a large dry bias is located over the central-eastern equatorial Pacific, where a slightly cold SST bias is simulated, which is deserving of further investigation. Reducing the bias of the precipitation mean state is one of the targets in the next phase of model development.

Under future global warming, precipitation is projected to increase in all SSP experiments because of the enhanced strength of the hydrological cycle, with the globally averaged precipitation increasing by 0.08, 0.12 and 0.18 mm d^{-1} in the SSP1-2.6, SSP2-4.5 and SSP5-8.5 experiments, respectively. The scaled precipitation changes by temperature changes yield about 2% of the precipitation increase per degree of global warming in all SSP experiments, which is consistent with prior studies (Li et al., 2013; Held and Soden, 2006). The spatial distribution of precipitation anom-

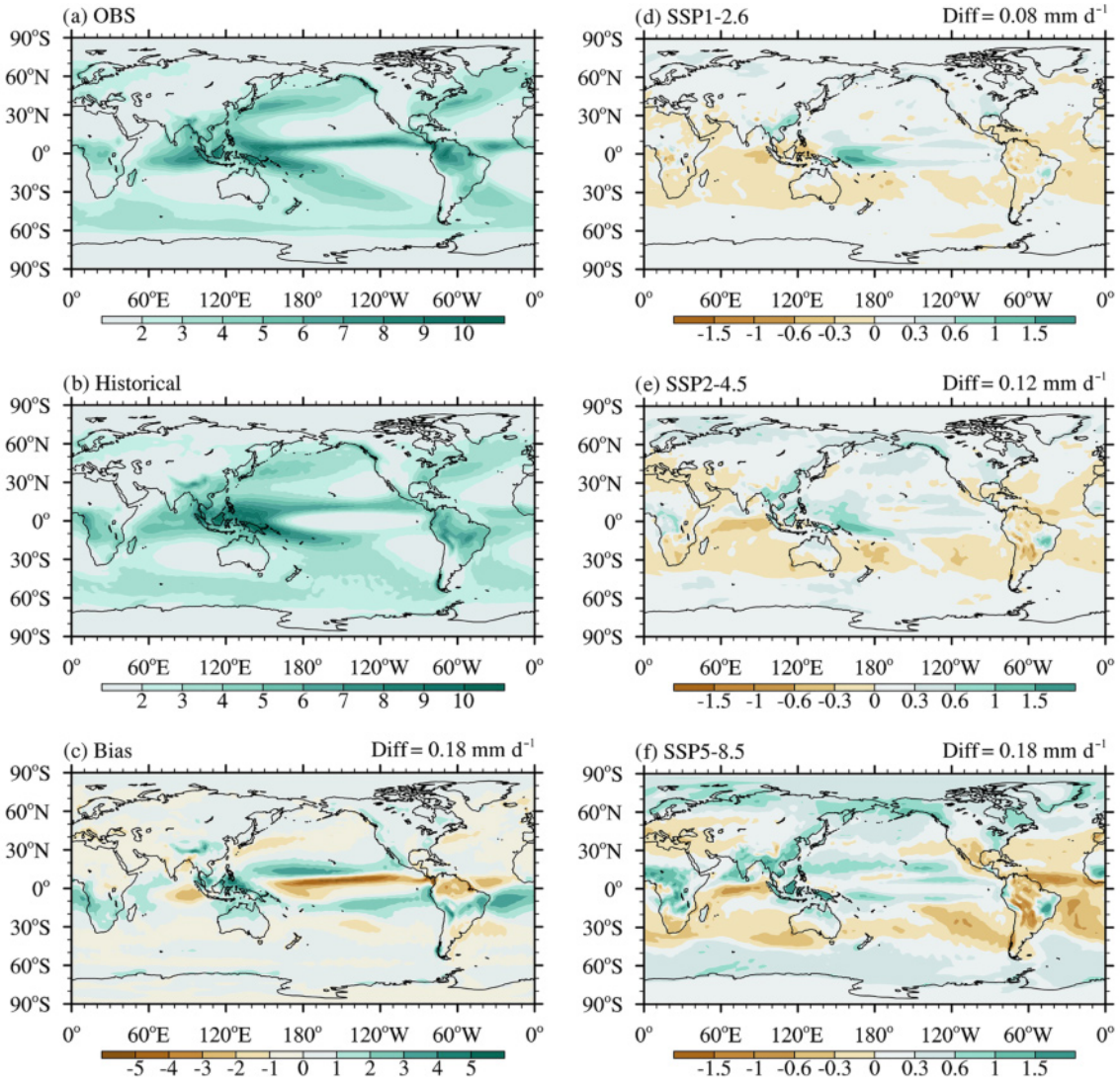

Fig. 4. As in Fig. 3 but for precipitation (units: mm d^{-1}).

alies shows that the increment of NH precipitation is greater than its SH counterpart, and the reduction in precipitation is more obvious over the SH subtropics than the NH subtropics. The hemispheric-averaged precipitation change over the NH is double that over the SH, probably due to the enlarged hemispheric thermal contrast and its associated enhanced cross-equatorial flow during boreal summer (not shown). Over the NH, the enhancement of precipitation is more robust over the Eastern Hemisphere (EH), especially over the North African and Asian monsoon regions. The enhanced EH monsoon precipitation could be due to the "warmer NH than SH" and "warmer land than ocean" patterns. The enlarged hemispheric and land–sea thermal contrasts can enhance the cross-equatorial flow and monsoon circulation over the EH (Lee and Wang, 2014; Cao and Zhao, 2020; Cao et al., 2020; Wang et al., 2020), leading to a greater increase in precipitation over the EH monsoon region (Figs. 4d–f). The projected precipitation is deficient over the tropical and subtropical Atlantic sector. Studies have suggested that the subtropics will become dryer under global warming owing to reduced moisture convergence (e.g., Chou and Neelin, 2004; Held and Soden, 2006). Wang et al. (2020) also pointed out that El Niño-like SST warming would enhance the subsidence over the American monsoon region. These two mechanisms might be responsible for the dryer tropical and subtropical Atlantic in NESM3. The details of the physical processes involved are deserving of further investigation. Over the tropics, the model projects enhanced precipitation over the equatorial Pacific and suppressed precipitation over the southern Indian Ocean.

3.4. *ENSO and MJO*

ENSO is one of the dominant internal variabilities of the Earth system; it modulates tropical and global teleconnections and is used as a prediction source on seasonal to interannual time scales (McPhaden et al., 2006). The observed and simulated ENSO variabilities are presented by the standard deviation of the December–February (DJF)-averaged SST anomaly over the tropical region in the observation and ensemble 1 of the historical experiment (Figs. 5a and b).

NESM3 reproduces well the spatial pattern of ENSO variability, with enhanced variability over the equatorial eastern Pacific (Fig. 5c). The simulated ENSO has a broad frequency range of between 2 and 7 years, agreeing well with the observations (figure not shown).

Compared to the modern climatology, all global warming experiments, SSP1-2.6, SSP2-4.5, and SSP5-8.5, project similar changes of ENSO variability (Figs. 5d–f). The amplitude of the SST variability is reduced over the central and eastern Pacific. The reduction of ENSO variability is more evident in the SSP5-8.5 experiment than in the other scenarios. This is consistent with previous studies that revealed about half of CMIP5 models project a decreased ENSO amplitude under the RCP8.5 scenario (e.g., Chen et al., 2015).

The MJO is a planetary-scale convectively coupled circulation system that affects the tropical climate and weather on the intraseasonal time scale (Waliser et al., 2003; Zhao et al., 2015a, b, 2018). Figure 6 compares the simulated and observed wavenumber-frequency spectra of 20–100 band-pass-filtered equatorial (10°S–10°N) precipitation. The observed MJO signal shows a distinct peak at wavenumbers 1–3 and a periodicity of about 30–60 days (Fig. 6a). The NESM3-simulated wavenumber and frequency characteristics resemble the observed MJO counterparts, as evidenced by the reasonable east–west propagation asymmetry, 30–90-day oscillation, and planetary-scale selection. However, the simulation tends to shift to a higher-frequency and smaller-scale oscillation than the observations (Fig. 6b). Under future global warming, NESM3 projects increased spectral power of precipitation anomalies and shortened MJO periodicity in all three Scenario MIP experiments (Figs. 6c–e). Indeed, previous studies have suggested amplification of the MJO variability under future global warming in models with superior MJO simulation capability (Rushley et al., 2019; Cui and Li, 2019).

4. Results from MH and LIG experiments

4.1. *Changes in solar insolation*

Abundant proxy records have revealed the existence of the current interglacial (Holocene) and most recent interglacial (LIG) periods (Marcott et al., 2013; Fischer et al., 2018). The numerical simulation of the MH has been conducted in all phases of PMIP, whist the LIG experiment is included in PMIP for the first time (Otto-Bliesner et al., 2017). Paleo-data synthesis has suggested that GMSTs during the MH/LIG were ~0.7/~1.0°C warmer than those of the PI period (Marcott et al., 2013; Fischer et al., 2018). The major driving force of MH and LIG climate changes is the changes in solar radiation, rather than changes in GHG forcing (Fig. 7), although GHG forcing is the primary driver of future anthropogenic warming (Otto-Bliesner et al., 2017). Comparative research on the two different types of warming climate provides a unique opportunity to understand the efficiency of different external forcing in changing the global climate. For example, Cao et al. (2019b) revealed that global monsoon precipitation efficacies are different under different external forcing, given the same impact in changing GMST.

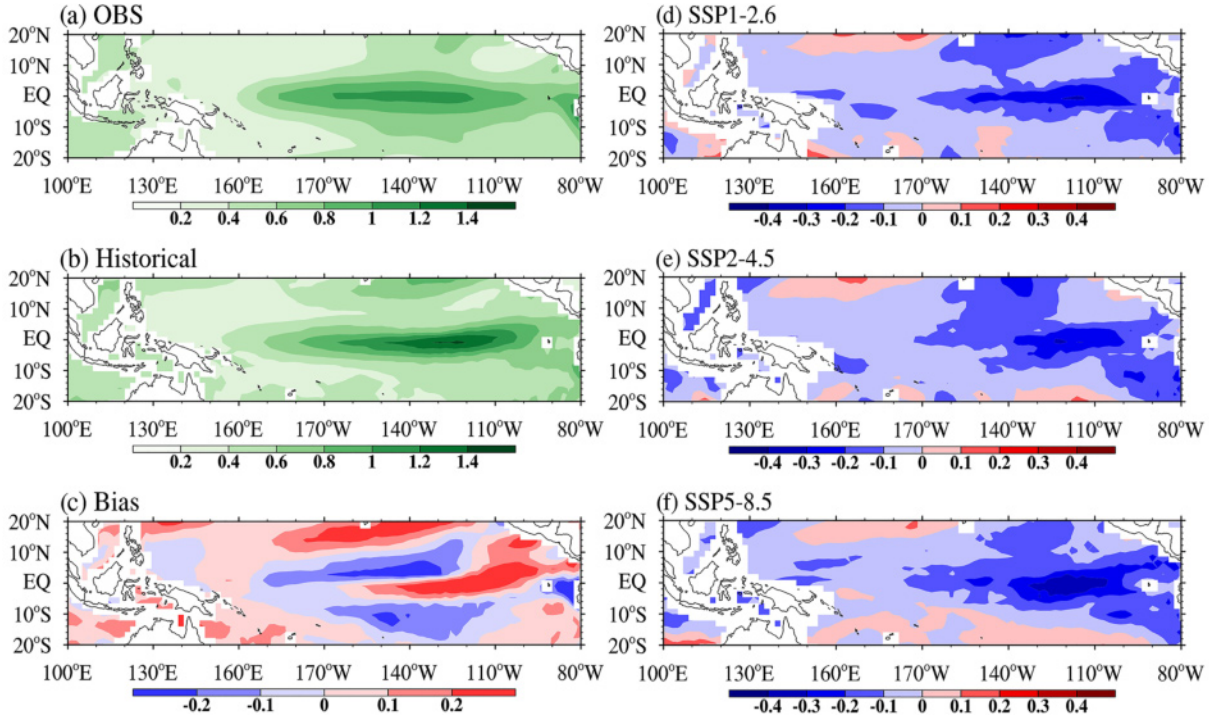

Fig. 5. Standard deviation of DJF-averaged SST (units: ℃) in the (a) observation, (b) realization 1 of the historical experiment, and (c) their differences. (d–f) Changes in standard deviation of the DJF-mean SST in realization 1 of the (d) SSP1-2.6, (e) SSP2-4.5 and (f) SSP5-8.5 experiments relative to realization 1 of the historical experiment.

Figure 7 shows the changes in top-of-the-atmosphere (TOA) irradiance during the MH and LIG periods. The change in TOA irradiance is larger in the higher latitudes than in the lower latitudes for both MH and LIG relative to

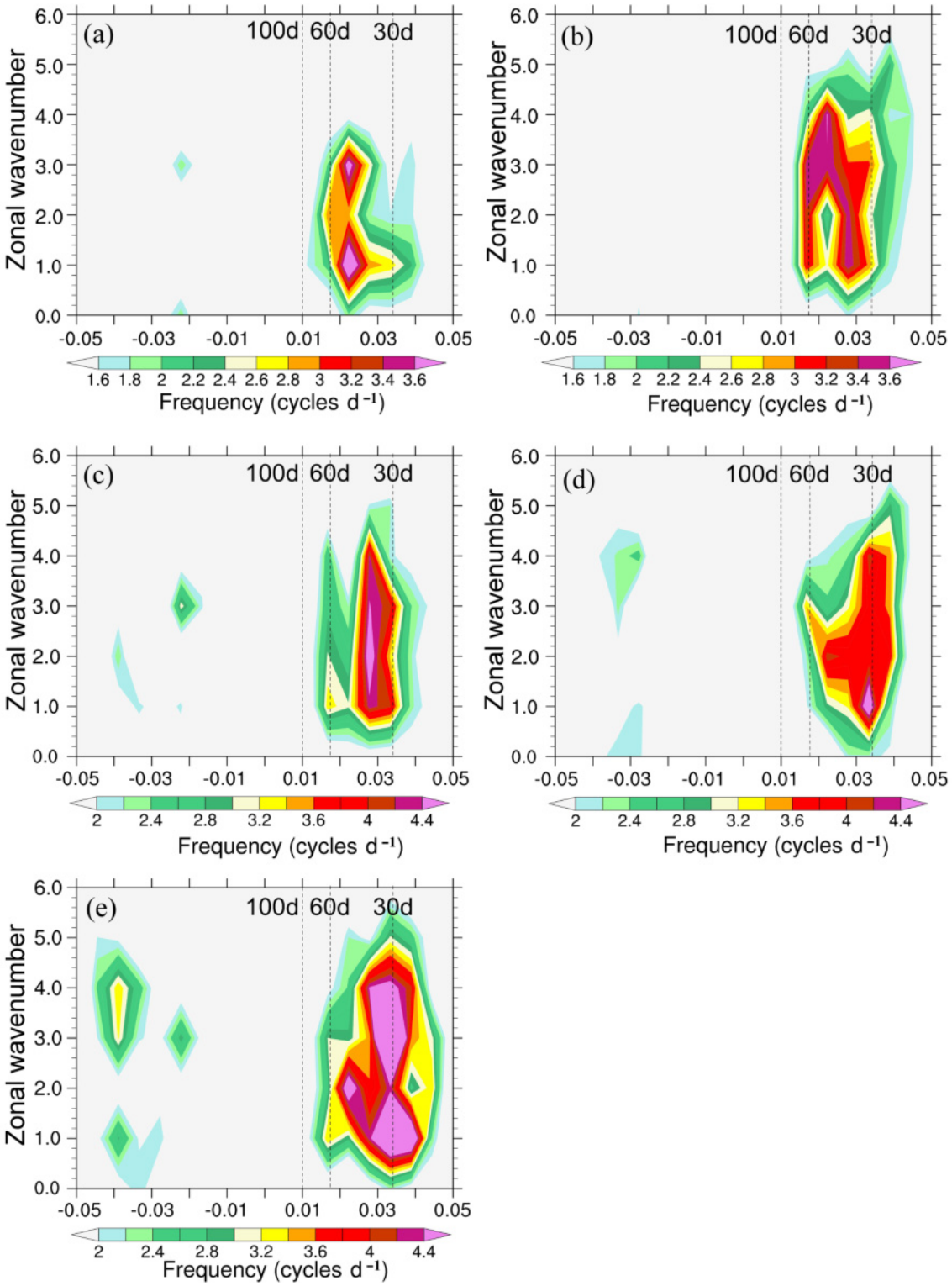

Fig. 6. Wavenumber–frequency spectra of spatiotemporally filtered precipitation (units: mm d^{-1}) in the boreal winter season (December–February) for the (a) observation, (b) historical experiment, and (c) SSP1-2.6, (d) SSP2-4.5 and (e) SSP5-8.5 experiments over the equatorial region (10°S–10°N). A 20–100-day bandpass filter was applied to the precipitation after removing its climatological seasonal cycle. The vertical dashed lines indicate the periods of 100 and 20 days, respectively. The period used in the observation and historical experiment is 1997–2014; and the period used for the SSP experiments is 2086–2100.

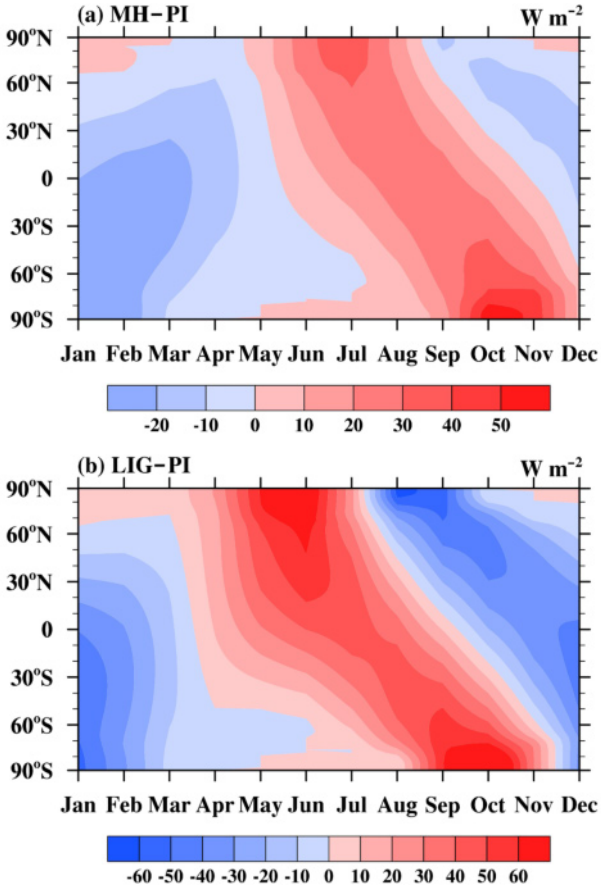

Fig. 7. Zonal-mean latitude–month insolation (units: W m^{-2}) changes in the (a) MH and (b) LIG experiments relative to the PI experiment.

PI. Over the NH, strengthened and weakened insolation are shown during June–September and November–April, respectively, in MH. Over the SH, the insolation is enhanced during July–November and weakened during January–April. The enhancement of TOA irradiance exceeds 30 W m^{-2} at high latitudes of both hemispheres during MH (Fig. 7a). In the LIG experiment, a positive/negative insolation anomaly is apparent during April–July/August–March over the majority of the NH. Over the SH, the pronounced changes in insolation are the reduced insolation during austral summer (December–March) and increased insolation during June–October (Fig. 7b). The reduction/increase of insolation can reach −40/50 W m^{-2} over the mid-to-high latitudes of both hemispheres during the LIG period (Fig. 7b). The changes in TOA solar radiation would enlarge the seasonal cycle of TOA irradiance, especially over the NH. In terms of the global mean value, the changes in globally averaged TOA irradiance are small during both the MH and LIG periods relative to the PI.

4.2. *Climatological temperature and precipitation*

In response to the change in TOA irradiance, the changes in global mean SAT are about −0.3°C and 0.1°C in the MH and LIG experiments (Figs. 8a and b), respectively, relative to the PI period. In the MH experiment, the change in SAT is generally less than 0.5°C over most of the globe, except for a large negative temperature response over the low-latitude landmass of the NH (Fig. 8a). This negative temperature anomaly is more obvious during boreal winter (Fig. 8e). During June–August (JJA), the SAT is increased over the midlatitudes of the NH continent due to the enhanced solar radiation (Figs. 7a and 8c). The enhanced seasonal contrast of SAT can also be attributed to the enlarged seasonal cycle of solar radiation over the NH.

The annual mean SAT change between the LIG and PI experiments is less than 1°C over most of the globe (Fig. 8b). The result is consistent with the PMIP4 multi-model ensemble (MME) results (Otto-Bliesner et al., 2020), although paleo-proxy data suggest a warmer climate compared to the simulations. The SAT anomaly pattern is characterized by cool SAT over the African and Asian monsoon regions and warm SAT over the Antarctic region (Fig. 8b). During boreal summer (JJA), warmer SAT appears over most of the global land surface, with maximum warming of 5°C over the midlatitude NH (Fig. 8d). During boreal winter (DJF), the land surface temperature during the LIG is cooler than during the PI period (Fig. 8f). Interestingly, the SAT response is opposite over the Barents Sea between the MH and LIG experiments (Figs. 8a and b), especially during the winter season (Figs. 8e and f). This difference in SAT responses may cause different climate impacts during the two periods, since extensive studies have emphasized the climate impacts of the sea-ice variability over the Barents Sea (Budikova, 2009; Vihma, 2014; Gao et al., 2015).

In summary, the changes in global mean SAT are small in the MH and LIG experiments compared to the PI experiment due to the small change in global mean TOA irradiance. However, the season cycles of SAT are enlarged in both the MH and LIG experiments because of the latitudinal and seasonal redistribution of TOA irradiance. The temperature responses simulated by NESM3 in the MH and LIG experiments are consistent with the PMIP4 MME mean.

In terms of precipitation, the anomalous patterns of annual mean precipitation are similar in the MH and LIG experiments, except for the larger magnitude in the LIG experiment. Over land, precipitation is enhanced over the NH monsoon regions, while it is decreased over the SH monsoon regions (Figs. 9a and b). Over the tropical ocean, precipitation is generally reduced, especially over the Pacific. This is due to the magnitude of precipitation change being larger in summer (Figs. 9c and d) than in winter (Figs. 9e and f), yielding the decreased annual mean precipitation in both the MH and LIG experiments. The anomalous patterns of precipitation during the MH and LIG periods in NESM3 are consistent with the MME mean of PMIP4 models (Scussolini et al., 2019; Brierley et al., 2020). Besides, the simulated precipitation anomaly is consistent with the proxy data over the NH continent, except for eastern Europe in the LIG experiment (Scussolini et al., 2019).

In JJA, precipitation is increased over the NH land

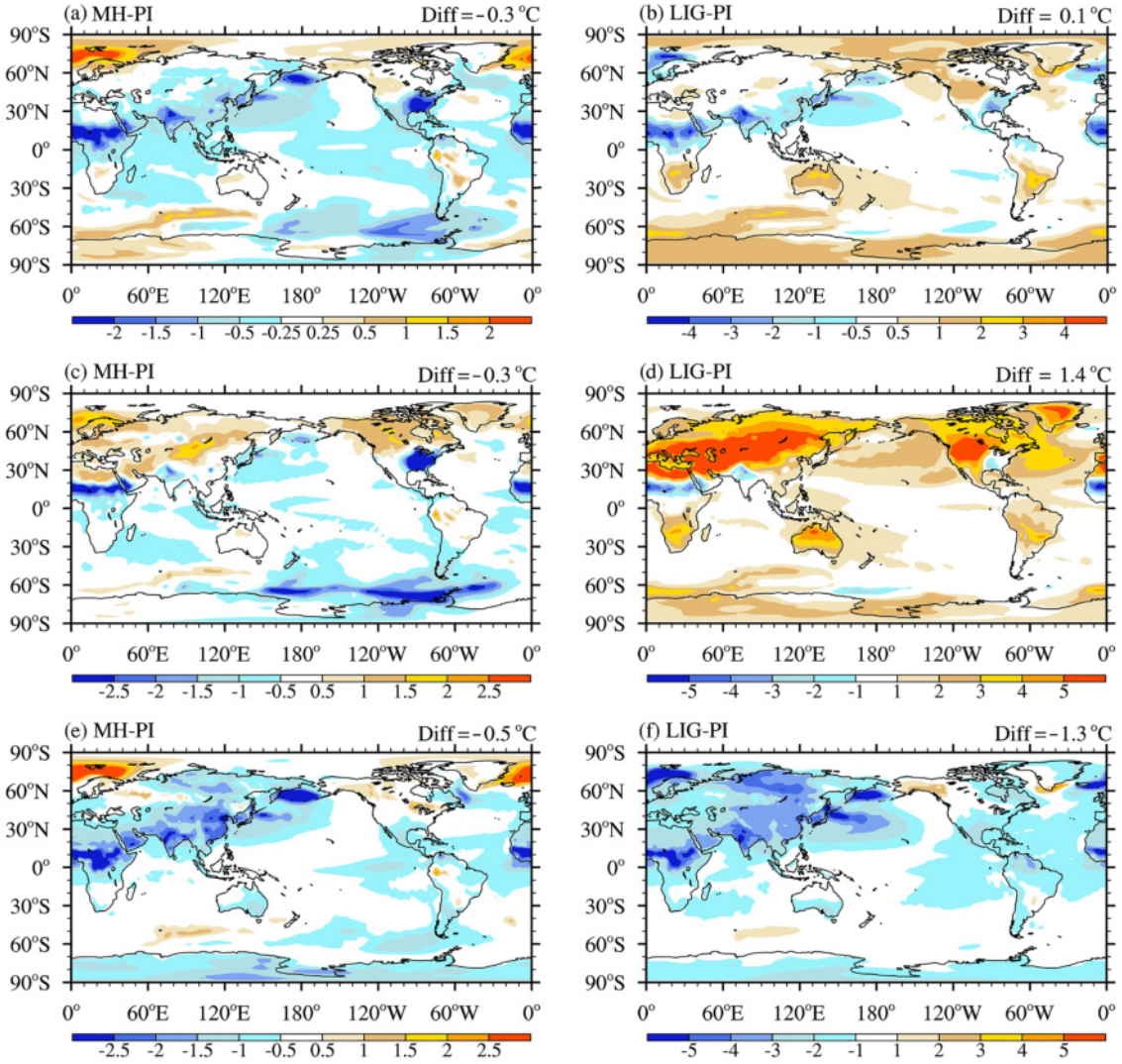

Fig. 8. SAT changes (units: ℃) in the (a, c, e) MH and (b, d, f) LIG experiments relative to the PI experiment: (a, b) annual mean; (c, d) JJA mean; (e, f) DJF mean. Note that different colorbars are used.

region, especially the monsoon region, but decreased over the Indo-Pacific region and southern equatorial Atlantic, in both the MH and LIG experiments (Figs. 9c and d). This could be attributable to the enhanced hemispheric thermal contrasts due to the larger warming over the NH mid-to-high latitudes. As suggested by Cao et al. (2020), the simulated enlarged meridional temperature gradient could induce a northward shift of the tropical rainband by altering the hemispheric energy transport and its associated Hadley circulation change (Figs. 8c and d). The changes in large-scale circulation drive the enhancement of moisture convergence over the NH monsoon region and weakening of moisture convergence over the Indo-Pacific region and southern equatorial Atlantic. Note that the summer monsoon precipitation changes over North Africa and Asia are enhanced under the solar radiative forcing and GHG forcing (Figs. 4d–f, Figs. 8c and d). In contrast, the responses of the North American summer monsoon precipitation are different for the two types of forcing. The associated underlying physical interpretation of these differences is beyond the scope of this study.

In DJF, NESM3 simulates a wetter tropical ocean but dryer austral continents in both the MH and LIG experiments (Figs. 9e and f). The weakened austral-summer monsoon precipitation over land is closely linked to the decreased land–sea thermal contrast and its associated weakened monsoon circulation (Figs. 8e and f, Figs. 9e and f).

4.3. *ENSO variability*

Given the uncertainty of projected changes in ENSO amplitude (Chen et al., 2015), examining paleo ENSO behavior provides a promising way to deepen our understanding of its physics, especially its responses to different SST mean states and different SST seasonal cycles (Brown et al., 2020). In this study, ENSO variability is defined by the standard deviation of DJF-mean SST in the central-eastern tropical Pacific. Figure 10 shows the changes in ENSO variability in the MH and LIG experiments relative to the PI experiment. The change in ENSO variability is small in the MH, while there is a noticeable decrease in ENSO variability under the LIG forcing (Fig. 10). The DJF SST standard devi-

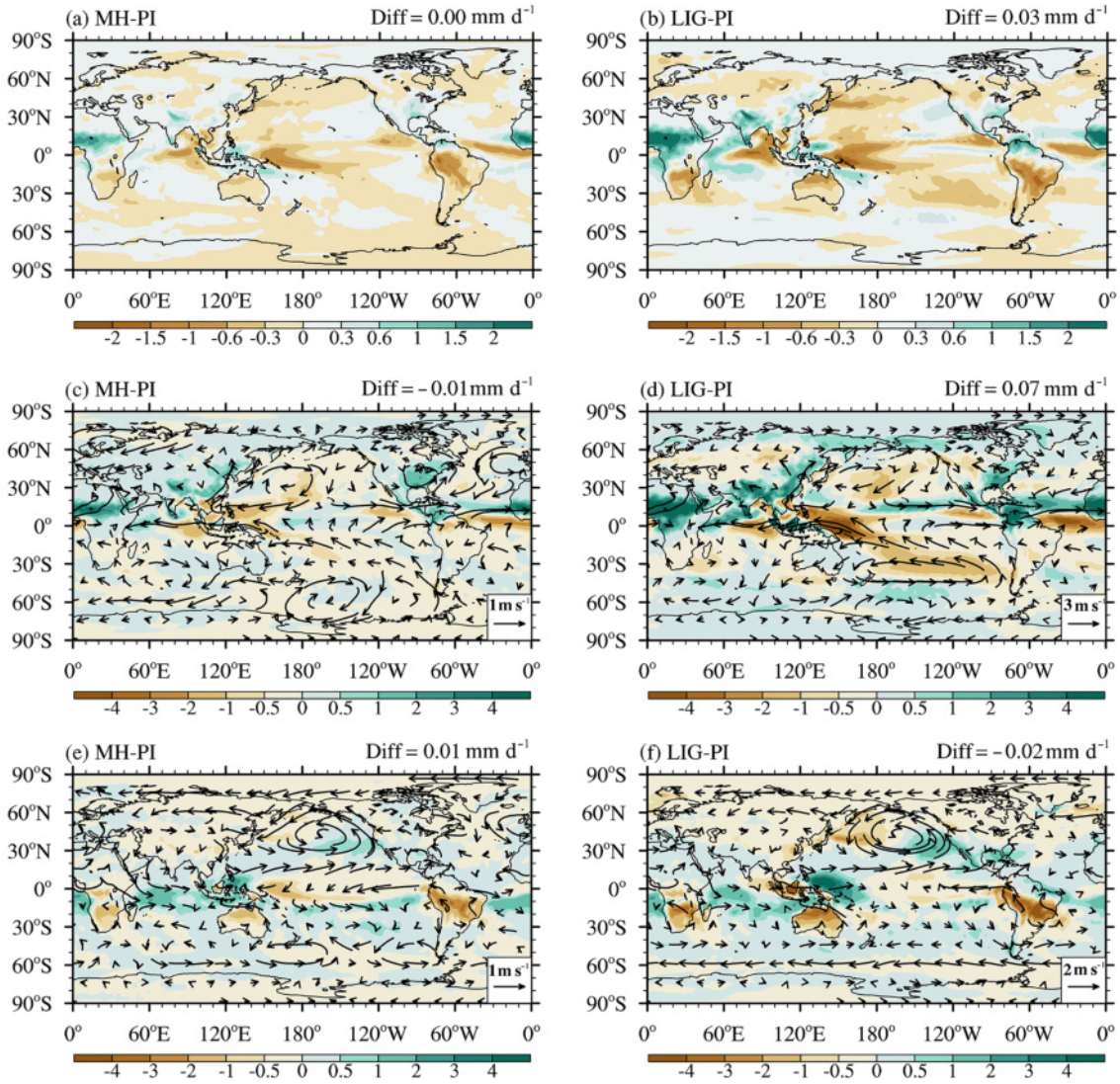

Fig. 9. Precipitation changes (units: mm d^{-1}) and 850-hPa circulation changes (units: m s^{-1}) in the (a, c, e) MH and (b, d, f) LIG experiments relative to the PI experiment: (a, b) annual mean; (c, d) JJA mean; (e, f) DJF mean.

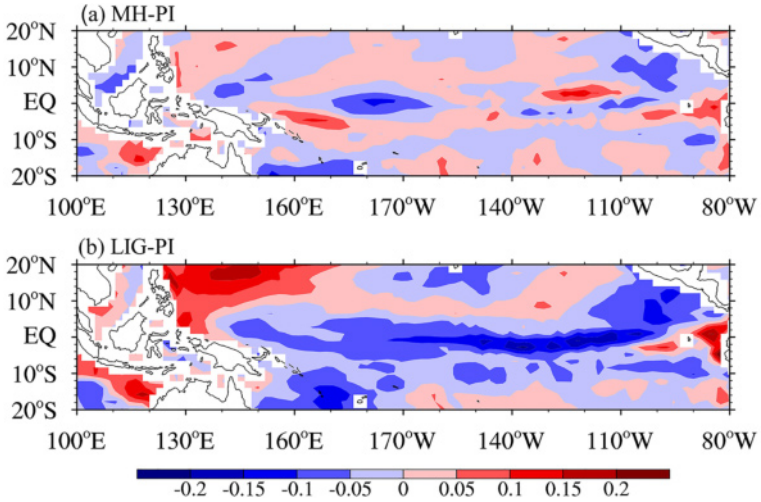

Fig. 10. Changes in DJF-averaged SST standard deviation (unit: ℃) in the (a) MH and (b) LIG experiments relative to the PI experiment.

ation is decreased in the central equatorial Pacific but increased in the eastern equatorial Pacific during MH. The averaged ENSO amplitudes in the Niño3.4 region are reduced in both the MH and LIG experiments. This result is consistent with the evidence from paleo-proxy data during the MH period and MH and LIG simulations from most PMIP4 models (Carré et al., 2014; Brown et al., 2020).

5. Experiment outputs

The NESM3 outputs were post-processed following the CMIP6 requirements, and have been submitted to the Earth System Grid Federation (ESGF) nodes. There are 48 variables for the atmosphere model (Table A1), 24 variables for the ocean model (Table A2), and 26 variables for the sea-ice model (Table A3). Detailed information regarding these variables in NESM3 is provided in the Appendix. Most of the variables in the atmosphere model are on pressure layers, while six and three variables are outputs on the model levels with frequencies of six-hourly and monthly, respectively. The model levels' pressures can be calculated using the following equation:

$$P_{(i,j,k)} = a_k P_0 + b_k P_{s(i,j)} ,$$

where $P_{(i,j,k)}$ is the derived pressure on model level interfaces, P_0 is 1013.25 hPa in NESM3, and $P_{s(i,j)}$ denotes the surface pressure of each model grid. The coefficients a_k and b_k indicate the hybrid level "A" and "B" coefficients on the interfaces, respectively (Giorgetta et al., 2013). The values of a_k and b_k are listed in the data files. The outputs from the ocean and sea-ice models are stored on the original model grids. They can be interpolated using tools like Climate Data Operators (https://code.mpimet.mpg.de/projects/cdo/embedded/cdo.pdf). All the model submissions are stored in the NetCDF (Network Common Data Form) format, which can be processed easily using appropriate software.

6. Summary

NESM3, a new member of the CMIP6 community, has performed the DECK, historical, Scenario MIP, and PMIP experiments for CMIP6. They include a 500-year PI experiment, a 150-year 1pctCO2 experiment, a 150-year abrupt4×CO2 experiment, five ensembles of historical experiments, two ensembles of SSP1-2.6, SSP2-4.5 and SSP5-8.5 experiments, a 100-year MH experiment, and a 100-year LIG experiment. All the outputs from these experiments have been submitted to the ESGF nodes to facilitate their download. In response to forcing in the form of an abrupt quadrupling of CO_2 and 1%yr^{-1} increase in CO_2, NESM3 simulates ECS and TCR values of 4.7 K and 2.8 K, respectively, which are slightly higher than the MME values of the CMIP6 models. Validation shows that NESM3 can reproduce reasonably well the temporal evolution of observed GMST, the climatological mean SAT, and precipitation, as well as the observed ENSO variability and MJO. Some common outstanding biases (e.g., double-ITCZ) still exist in NESM3.

The projected climatological SAT and precipitation show similar changes for all three Scenario MIP experiments, but with different amplitudes. The change in SAT shows clear "NH warmer than SH" and "land warmer than ocean" patterns, as well as the El Niño-like SST warming in the tropics. Shaped by this SAT pattern, the projected NH precipitation is increased more than the SH precipitation, and EH precipitation is enhanced more than the western hemisphere precipitation. This precipitation pattern is closely linked to the large-scale circulation change due to large-scale differential SAT warming. The projected summertime Arctic SIE declines rapidly, and the Arctic summer will be sea-ice-free by around 2034, 2036 and 2027 in SSP1-2.6, SSP2-4.5 and SSP5-8.5, respectively. In the three SSP experiments, all projections of ENSO amplitude are found to decrease in the central and eastern tropical Pacific.

Two paleoclimate simulations, i.e., the MH and LIG experiments, were conducted following the experimental design of PMIP4. The simulated changes in SAT are in line with the changes in TOA irradiance for both experiments. These are characterized by an enhanced seasonal contrast of temperature over the NH, especially over land. Correspondingly, enhanced NH monsoon precipitation over land and suppressed precipitation over the majority of the tropics are seen. Changes in temperature and precipitation are closely consistent with those of other CMIP6/PMIP4 models and proxy data. Additionally, a decreased ENSO amplitude under the LIG forcing can be seen in NESM3.

Acknowledgements. This work was jointly supported by the Natural Science Foundation of China of Jiangsu Province (Grant No. BK20180812, BK20181412), the National Natural Science Foundation of China (Grant No. 42005017, 41675072, 41922033), and the Startup Foundation for Introducing Talent of NUIST (Grant No. 2018r063). We acknowledge the computer resources at the NUIST High Performance Computer Center. This is ESMC publication NO. 330.

Data availability

The datasets of the DECK, historical, Scenario MIP, and PMIP experiments are available at https://esgf-node.llnl.gov/search/cmip6/.

Open Access This article is distributed under the terms of the Creative Commons Attribution 4.0 International License (http://creativecommons.org/licenses/by/4.0/), which permits unrestricted use, distribution, and reproduction in any medium, provided you give appropriate credit to the original author(s) and the source, provide a link to the Creative Commons license, and indicate if changes were made.

APPENDIX

The submitted variables in the atmospheric, ocean and sea-ice model components are listed in Tables A1, A2 and A3, respectively. The "Variable" and "Description" columns present the output name and its detailed description in the CMIP6 archive, respectively. The "Frequency" column is the submission data frequencies.

Table A1. Atmospheric model output variables. The notation "6hrLev" in the frequency column indicates the variables are outputted over model levels.

Variable	Frequency	Description
cl	monthlyLev	cloud cover
cli	monthlyLev	mass fraction of cloud ice
clivi	monthly	ice water path
clt	monthly, daily, 3 h	total cloud cover
clw	monthlyLev	mass fraction of cloud liquid water
clwvi	monthly	condensed water path
evspsbl	monthly	evaporation
hfls	monthly, daily, 3 h	surface upward latent heat flux
hfss	monthly, daily, 3 h	surface upward sensible heat flux
hur	monthly, daily	relative humidity
hus	monthly, daily, 6hrLev	specific humidity
pr	monthly, daily, 3 h	precipitation
prc	monthly, daily, 3 h	convective precipitation
prsn	monthly, daily, 3 h	snowfall flux
prw	monthly	water vapor path
ps	monthly, daily, 6hrLev	surface air pressure
psl	monthly, daily, 6 h	sea level pressure
rlds	monthly, daily, 3 h	surface downwelling longwave radiation
rldscs	monthly, 3 h	surface downwelling clear-sky longwave radiation
rlus	monthly, daily, 3 h	surface upwelling longwave radiation
rlut	monthly, daily	TOA outgoing longwave radiation
rlutcs	monthly	TOA outgoing clear-sky longwave radiation
rsds	monthly, daily, 3 h	surface downwelling shortwave radiation
rsdscs	monthly, 3 h	surface downwelling clear-sky shortwave radiation
rsdt	monthly	TOA incident shortwave radiation
rsus	monthly, daily, 3 h	surface upwelling shortwave radiation
rsuscs	monthly, 3 h	surface upwelling clear-sky shortwave radiation
rsut	monthly	top-of-atmosphere outgoing shortwave radiation
rsutcs	monthly	TOA outgoing clear-sky shortwave radiation
rv850	6 h	relative vorticity at 850 hPa
sfcWindmax	daily	daily maximum near-surface wind speed
snw	daily	surface snow amount
ta	monthly, daily, 6 h, 6hrLev	air temperature
tas	monthly, daily, 3 h	near-surface air temperature
tasmax	monthly, daily	daily minimum near-surface air temperature
tasmin	monthly, daily	daily maximum near-surface air temperature
tauu	monthly	surface downward eastward wind stress
tauv	monthly	surface downward northward wind stress
tos	3 h	sea surface temperature
ts	monthly	surface temperature
tslsi	daily,3 h	surface temperature where land or sea ice
ua	monthly, daily, 6 h, 6hrlev	eastward wind
uas	monthly, daily, 3 h	eastward near-surface wind
va	monthly, daily, 6 h, 6hrlev	northward wind
vas	monthly, daily, 3 h	northward near-surface wind
wap	monthly, daily	omega (=dp/dt)
zg	monthly	geopotential height
zg500	6 h	geopotential height at 500 hPa

Table A2. Ocean model output variables.

Variable	Frequency	Description
tos	monthly, daily	sea surface temperature
tauuo	monthly	surface downward *X* stress
sos	monthly	sea surface salinity
wo	monthly	sea water vertical velocity
thetao	monthly	sea water potential temperature
wfo	monthly	water flux into sea water
tauvo	monthly	surface downward *Y* stress
vo	monthly	sea water *Y* velocity
hfds	monthly	downward heat flux at sea water surface
uo	monthly	sea water *X* velocity
rsntds	monthly	net downward shortwave radiation at sea water surface
zos	monthly	sea surface height above geoid
so	monthly	sea water salinity
mlotst	monthly	ocean mixed layer thickness defined by sigma *T*

Table A3. Sea ice model output variables.

Variable	Frequency	Description
siconc	monthly, daily	sea ice area fraction
sidconcdyn	monthly	tendency_of_sea_ice_area_fraction_due_to_dynamics
sidconcth	monthly	tendency_of_sea_ice_area_fraction_due_to_thermodynamics
siflfwdrain	monthly	freshwater_flux_from_ice_surface
sifllatstop	monthly	surface_upward_latent_heat_flux
sifllwdtop	monthly	surface_downwelling_longwave_flux_in_air
siflsenstop	monthly	surface_upward_sensible_heat_flux
siflswdtop	monthly	surface_downwelling_shortwave_flux_in_air
siflswutop	monthly	surface_upwelling_shortwave_flux_in_air
siforcecoriolx	monthly	coriolis_force_on_sea_ice_x
siforcecorioly	monthly	coriolis_force_on_sea_ice_y
siforcetiltx	monthly	sea_surface_tilt_force_on_sea_ice_x
siforcetilty	monthly	sea_surface_tilt_force_on_sea_ice_y
siitdconc	monthly	sea_ice_area_fraction_over_categories
siitdthick	monthly	sea_ice_thickness_over_categories
sisnthick	monthly	surface_snow_thickness
sistrxdtop	monthly	surface_downward_x_stress
sistrxubot	monthly	upward_x_stress_at_sea_ice_base
sistrydtop	monthly	surface_downward_y_stress
sistryubot	monthly	upward_y_stress_at_sea_ice_base
sitemptop	monthly	sea_ice_surface_temperature
sithick	monthly, daily	sea_ice_thickness
sitimefrac	monthly	sea_ice_time_fraction
siu	monthly, daily	sea_ice_x_velocity
siv	monthly, daily	sea_ice_y_velocity
sndmassi	monthly	tendency_of_surface_snow_amount_due_to_conversion_of_snow_to_sea_ice

REFERENCES

Brierley, C. M., and Coauthors, 2020: Large-scale features and evaluation of the PMIP4-CMIP6 *midHolocene* simulations. *Climate of the Past*, **16**, 1847–1972, https://doi.org/10.5194/cp-16-1847-2020.

Brovkin, V., L. Boysen, T. Raddatz, V. Gayler, A. Loew, and M. Claussen, 2013: Evaluation of vegetation cover and land-surface albedo in MPI-ESM CMIP5 simulations. *Journal of Advances in Modeling Earth Systems*, **5**, 48–57, https://doi.org/10.1029/2012MS000169.

Brown, J., R. and Coauthors, 2020: Comparison of past and future simulations of ENSO in CMIP5/PMIP3 and CMIP6/PMIP4 models. *Climate of the Past*, **16**, 1777–1805, https://doi.org/10.5194/cp-16-1777-2020.

Budikova, D., 2009: Role of Arctic sea ice in global atmospheric circulation: A review. *Global and Planetary Change*, **68**, 149–163, https://doi.org/10.1016/j.gloplacha.2009.04.001.

Cao, J., and H. K. Zhao, 2020: Distinct response of Northern Hemisphere land monsoon precipitation to transient and stabilized warming scenarios. *Advances in Climate Change Research*, **11**, 161–171, https://doi.org/10.1016/j.accre.2020.09.007.

Cao, J., and Coauthors, 2018: The NUIST Earth System Model (NESM) version 3: Description and preliminary evaluation. *Geoscientific Model Development*, **11**, 2975–2993, https://doi.org/10.5194/gmd-11-2975-2018.

Cao, J., B. Wang, and J. Liu, 2019a: Attribution of the last glacial maximum climate formation. *Climate Dyn.*, **53**, 1661–1679, https://doi.org/10.1007/s00382-019-04711-6.

Cao, J., B. Wang, and L. B. Ma, 2019b: Attribution of global monsoon response to the last glacial maximum forcings. *J. Climate*, **32**, 6589–6605, https://doi.org/10.1175/JCLI-D-18-0871.1.

Cao, J., B. Wang, B. Q. Xiang, J. Li, T. J. Wu, X. H. Fu, L. G. Wu, and J. Z. Min, 2015: Major modes of short-term climate variability in the newly developed NUIST Earth System Model (NESM). *Adv. Atmos. Sci.*, **32**, 585–600, https://doi.org/10.1007/s00376-014-4200-6.

Cao, J., B. Wang, B. Wang, H. Zhao, C. Wang, Y. Han, 2020: Sources of the Intermodel Spread in Projected Global Monsoon Hydrological Sensitivity. *Geophysical Research Letters*, **47**, e2020GL089560, https://doi.org/10.1029/2020GL089560.

Capron, E., A. Govin, R. Feng, B. L. Otto-Bliesner, and E. W. Wolff, 2017: Critical evaluation of climate syntheses to benchmark CMIP6/PMIP4 127 ka Last Interglacial simulations in the high-latitude regions. *Quaternary Science Reviews*, **168**, 137–150, https://doi.org/10.1016/j.quascirev.2017.04.019.

Chen. L., T. Li, and Y. Q. Yu, 2015: Causes of strengthening and weakening of ENSO amplitude under global warming in four CMIP5 models. *J. Climate*, **28**, 3250–3274, https://doi.org/10.1175/JCLI-D-14-00439.1.

Chou, C., and J. D. Neelin, 2004: Mechanisms of global warming impacts on regional tropical precipitation. *J. Climate*, **17**, 2688–2701, https://doi.org/10.1175/1520-0442(2004)017<2688:MOGWIO>2.0.CO;2.

Collins, M., and Coauthors, 2013: Long-term climate change: Projections, commitments and irreversibility. *Climate Change 2013: The Physical Science Basis. Contribution of Working Group I to the Fifth Assessment Report of the Intergovernmental Panel on Climate Change*, T. F. Stocker et al., Cambridge University Press, Cambridge, United Kingdom and New York, NY, USA.

Carré, M., and Coauthors, 2014: Holocene history of ENSO variance and asymmetry in the eastern tropical Pacific. *Science*, **345**, 1045–1048, https://doi.org/10.1126/science.1252220.

Cui, J. X., and T. Li, 2019: Changes of MJO propagation characteristics under global warming. *Climate Dyn.*, **53**, 5311–5327, https://doi.org/10.1007/s00382-019-04864-4.

Eyring, V., S. Bony, G. A. Meehl, C. A. Senior, B. Stevens, R. J. Stouffer, and K. E. Taylor, 2016: Overview of the Coupled Model Intercomparison Project Phase 6(CMIP6) experimental design and organization. *Geoscientific Model Development*, **9**, 1937–1958, https://doi.org/10.5194/gmd-9-1937-2016.

Fischer, H., and Coauthors, 2018: Palaeoclimate constraints on the impact of 2°C anthropogenic warming and beyond. *Nature Geoscience*, **11**, 474–485, https://doi.org/10.1038/s41561-018-0146-0.

Flato, G., and Coauthors, 2013: Evaluation of climate models. *Climate Change 2013: The Physical Science Basis. Contribution of Working Group I to the Fifth Assessment Report of the Intergovernmental Panel on Climate Change*, T. F. Stocker et al., Eds., Cambridge University Press, Cambridge, United Kingdom and New York, NY, USA, 817-821.

Gao, Y., and Coauthors, 2015: Arctic sea ice and Eurasian climate: A review. *Adv. Atmos. Sci.*, **32**, 92–114, https://doi.org/10.1007/s00376-014-0009-6.

Giorgetta, M. A., and Coauthors, 2013: The atmospheric general circulation model ECHAM6: Model description. Technical Report 135, Max Planck Institute for Meteorology, Hamburg, Germany.

Gregory, J. M., and coauthors, 2004: A new method for diagnosing radiative forcing and climate sensitivity. *Geophys. Res. Lett.*, **31**, L03205, https://doi.org/10.1029/2003GL018747.

Held, I. M., and B. Soden, 2006: Robust responses of the hydrological cycle to global warming. *J. Climate*, **19**, 5686–5699, https://doi.org/10.1175/JCLI3990.1.

Hoffman, J. S., P. U. Clark, A. C. Parnell, and F. He, 2017: Regional and global sea-surface temperatures during the last interglaciation. *Science*, **355**, 276–279, https://doi.org/10.1126/science.aai8464.

Huffman, G. J., R. F. Adler, D. T. Bolvin, and G. J. Gu, 2009: Improving the global precipitation record: GPCP version 2.1. *Geophys. Res. Lett.*, **36**, L17808, https://doi.org/10.1029/2009GL040000.

Hunke, E. C., W. H. Lipscomb, 2010: *CICE: The Los Alamos Sea Ice Model Documentation and Software User's Manual Version 4.1*. LA-CC-06-012, T-3 Fluid Dynamics Group, Los Alamos National Laboratory, Los Alamos, NM.

IPCC, 2013: Climate Change 2013: The Physical Science Basis. Contribution of Working Group I to the Fifth Assessment Report of the Intergovernmental Panel on Climate Change, Stocker et al., Eds., *IPCC Fifth Assessment Report*. Cambridge, Cambridge University Press, Cambridge, United Kingdom and New York, NY, USA, 1535 pp, https://doi.org/10.1017/CBO9781107415324.

Jahn, A., J. E. Kay, M. M. Holland, and D. M. Hall, 2016: How predictable is the timing of a summer ice-free Arctic? Geophys *Res. Lett.*, **43**, 9113–9120, https://doi.org/10.1002/2016GL070067.

Joussaume, S., and K. Taylor, 1995: Status of the Paleoclimate Modeling Intercomparison Project. *Proc First International AMIP Scientific Conference*, Geneva, World Meteorology Organization, Monterey, USA, 425-430.

Kanamitsu, M., W. Ebisuzaki, J. Woollen, S. K. Yang, J. J. Hnilo, M. Fiorino, and G. L. Potter, 2002: NCEP-DOE AMIP-II Reanalysis (R-2). *Bull. Amer. Meteor. Soc.*, **83**, 1631–1644, https://doi.org/10.1175/BAMS-83-11-1631.

Lee, J. Y., and B. Wang, 2014: Future change of global monsoon in the CMIP5. *Climate Dyn.*, **42**, 101–119, https://doi.org/10.1007/s00382-012-1564-0.

Li, G., S. P. Harrison, P. J. Bartlein, K. Izumi, and I. C. Prentice, 2013: Precipitation scaling with temperature in warm and cold climates: An analysis of CMIP5 simulations. *Geophys. Res. Lett.*, **40**, 4018–4024, https://doi.org/10.1002/grl.50730.

Ma, L., B. Wang, and J. Cao, 2020: Impacts of atmosphere-sea ice-ocean interaction on Southern Ocean deep convection in a climate system model. *Climate Dyn.*, **54**, 4075–4093, https://doi.org/10.1007/s00382-020-05218-1.

Madec, G., and the NEMO team, 2012: NEMO ocean engine. Note du pole de modélisation de l'Institut Pierre-Simon Laplace. No 27, Institut Pierre-Simon Laplace (IPSL), France.

Marcott, S. A., J. D. Shakun, P. U. Clark, and A. C. Mix, 2013: A reconstruction of regional and global temperature for the past 11, 300 years. *Science*, **399**, 1198–1201, https://doi.org/10.1126/science.1228026.

Massonnet, F., T. Fichefet, H. Goosse, C. M. Bitz, G. Philippon-Berthier, M. M. Holland, and P.-Y. Barriat, 2012: Constraining projections of summer Arctic sea ice. *The Cryosphere*, **6**, 1383–1394, https://doi.org/10.5194/tc-6-1383-2012.

McPhaden, M. J., S. E. Zebiak, and M. H. Glantz, 2006: ENSO as an integrating concept in Earth science. *Science*, **314**, 1740–1745, https://doi.org/10.1126/science.1132588.

Meehl, G. A., C. A. Senior, V. Eyring, G. Flato, J.-F. Lamarque, R. J. Stouffer, K. E. Taylor, and M. Schlund, 2020: Context for interpreting equilibrium climate sensitivity and transient climate response from the CMIP6 Earth system models. *Science Advances*, **6**, eaba1981, https://doi.org/10.1126/sciadv.aba1981.

Meehl, G. A., G. J. Boer, C. Covey, M. Latif, and R. J. Stouffer, 2000: The Coupled Model Intercomparison Project (CMIP). *Bull. Amer. Meteor. Soc.*, **81**, 313–318, https://doi.org/10.1175/1520-0477(2000)081<0313:TCMIPC>2.3.CO;2.

Morice, C. P., J. J. Kennedy, N. A. Rayner, and P. D. Jones, 2012: Quantifying uncertainties in global and regional temperature change using an ensemble of observational estimates: The HadCRUT4 data set. *J. Geophys. Res. Atmos.*, **117**, D08101, https://doi.org/10.1029/2011JD017187.

O'Neill, B. C. and Coauthors, 2016: The Scenario Model Intercomparison Project (ScenarioMIP) for CMIP6. *Geoscientific Model Development*, **9**, 3461–3482, https://doi.org/10.5194/gmd-9-3461-2016.

Otto-Bliesner, B. L., and Coauthors, 2017: The PMIP4 contribution to CMIP6-Part 2: Two interglacials, scientific objective and experimental design for Holocene and Last Interglacial simulations. *Geoscientific Model Development*, **10**, 3979–4003, https://doi.org/10.5194/gmd-10-3979-2017.

Otto-Bliesner, B. L., and Coauthors, 2020: Large-scale features of last interglacial climate: Results from evaluating the *lig127k* simulations for CMIP6-PMIP4. *Climate of the Past*, https://doi.org/10.5194/cp-2019-174. (in press)

Overland, J. E., and M. Y. Wang, 2013: When will the summer Arctic be nearly sea ice free? Geophys *Res. Lett.*, **40**, 2097–2101, https://doi.org/10.1002/grl.50316.

Rayner, N. A., D. E. Parker, E. B. Horton, C. K. Folland, L. V. Alexander, D. P. Rowell, E. C. Kent, and A. Kaplan, 2003: Global analyses of sea surface temperature, sea ice, and night marine air temperature since the late nineteenth century. *J. Geophys. Res. Atmos.*, **108**, 4407, https://doi.org/10.1029/2002JD002670.

Rushley, S., D. Kim, and Á. F. Adames, 2019: Changes in the MJO under greenhouse gas-induced warming in CMIP5 models. *J. Climate*, **32**, 803–821, https://doi.org/10.1175/JCLI-D-18-0437.1.

Scussolini, P., and Coauthors, 2019: Agreement between reconstructed and modeled boreal precipitation of the Last Interglacial. *Science Advances*, **5**, eaax7047, https://doi.org/10.1126/sciadv.aax7047.

Twomey, S., 1977: The influence of pollution on the shortwave albedo of clouds. *Journal of Atmospheric Science*, **34**, 1149–1152, https://doi.org/10.1175/1520-0469(1977)034<1149:TIOPOT>2.0.CO;2.

Valcke, S. T. Craig, and L. Coquart, 2015: OASIS3-MCT User Guide, OASIS3-MCT 3.0. CERFACS Technical Report, CERFACS TR/CMGC/15/38, Toulouse, France. Available from http://www.cerfacs.fr/oa4web/oasis3-mct_3.0/oasis3mct_UserGuide.pdf, 2015.

Vihma, T., 2014: Effects of Arctic Sea ice decline on weather and climate: A review. *Surveys in Geophysics*, **35**, 1175–1214, https://doi.org/10.1007/s10712-014-9284-0.

Waliser, D. E., K. M. Lau, W. Stern, and C. Jones, 2003: Potential predictability of the madden-Julian oscillation. *Bull. Amer. Meteor. Soc.*, **84**, 33–50, https://doi.org/10.1175/BAMS-84-1-33.

Wang, B., C. H. Jin, and J. Liu, 2020: Understanding future change of global monsoons projected by CMIP6 models. *J. Climate*, **33**, 6471–6489, https://doi.org/10.1175/JCLI-D-19-0993.1.

Wang, B., and coauthors, 2018: Toward predicting changes in the land monsoon rainfall a decade in advance. *J. Climate*, **31**, 2699–2714, https://doi.org/10.1175/JCLI-D-17-0521.1.

Yin, Q. Z., and A. Berger, 2015: Interglacial analogues of the Holocene and its natural near future. *Quaternary Science Reviews*, **120**, 28–46, https://doi.org/10.1016/j.quascirev.2015.04.008.

Zelinka, M. D., T. A. Myers, D. T. McCoy, S. Po - Chedley, P. M. Caldwell, P. Ceppi, S. A. Klein, and K. E. Taylor, 2020: Causes of higher climate sensitivity in CMIP6 models. *Geophys. Res. Lett.*, **47**, e2019GL085782, https://doi.org/10.1029/2019GL085782.

Zhao, H. K., R. Yoshida, and G. B. Raga, 2015a: Impact of the madden-Julian oscillation on western north pacific tropical cyclogenesis associated with large-scale patterns. *Journal of Applied Meteorology Climatology*, **54**, 1413–1429, https://doi.org/10.1175/JAMC-D-14-0254.1.

Zhao, H. K., X. N. Jiang, and L. G. Wu, 2015b: Modulation of northwest pacific tropical cyclone genesis by the intraseasonal variability. *Journal of the Meteorological Society of Japan. Ser. II*, **93**, 81–97, https://doi.org/10.2151/jmsj.2015-006.

Zhao H. K., S. H. Chen, P. J. Klotzbach, and G. B. Raga, 2018: Impact of the extended boreal summer intraseasonal oscillation on western north pacific tropical cloud cluster genesis productivity. *J. Climate*, **31**, 9175–9191, https://doi.org/10.1175/JCLI-D-18-0113.1.